JOURNAL OF SYNCHROTRON RADIATION
ISSN 1600-5775

Potential of propagation-based synchrotron X-ray phase-contrast computed tomography for cardiac tissue engineering

Mohammad Izadifar,[a,b,c,d]* Paul Babyn,[a,e] Dean Chapman,[a,f] Michael E. Kelly[a,b,c] and Xiongbiao Chen[a,d]

[a]Division of Biomedical Engineering, College of Engineering, University of Saskatchewan, Saskatoon, SK, Canada, [b]Saskatchewan Cerebrovascular Centre, Royal University Hospital, Saskatoon, SK, Canada, [c]Department of Surgery, College of Medicine, University of Saskatchewan, Saskatoon, SK, Canada, [d]Department of Mechanical Engineering, College of Engineering, University of Saskatchewan, Saskatoon, SK, Canada, [e]Department of Medical Imaging, College of Medicine, University of Saskatchewan, Saskatoon, SK, Canada, and [f]Department of Anatomy and Cell Biology, College of Medicine, University of Saskatchewan, Saskatoon, SK, Canada. *Correspondence e-mail: mohammad.izadifar@usask.ca

Received 21 January 2017
Accepted 24 April 2017

Edited by A. F. Craievich, University of São Paulo, Brazil

Keywords: cardiac patch; computed tomography; hydrogel; phase-contrast imaging; tissue engineering.

Hydrogel-based cardiac tissue engineering offers great promise for myocardial infarction repair. The ability to visualize engineered systems *in vivo* in animal models is desired to monitor the performance of cardiac constructs. However, due to the low density and weak X-ray attenuation of hydrogels, conventional radiography and micro-computed tomography are unable to visualize the hydrogel cardiac constructs upon their implantation, thus limiting their use in animal systems. This paper presents a study on the optimization of synchrotron X-ray propagation-based phase-contrast imaging computed tomography (PCI-CT) for three-dimensional (3D) visualization and assessment of the hydrogel cardiac patches. First, alginate hydrogel was 3D-printed into cardiac patches, with the pores filled by fibrin. The hydrogel patches were then surgically implanted on rat hearts. A week after surgery, the hearts including patches were excised and embedded in a soft-tissue-mimicking gel for imaging by using PCI-CT at an X-ray energy of 25 keV. During imaging, the sample-to-detector distances, CT-scan time and the region of interest (ROI) were varied and examined for their effects on both imaging quality and radiation dose. The results showed that phase-retrieved PCI-CT images provided edge-enhancement fringes at a sample-to-detector distance of 147 cm that enabled visualization of anatomical and microstructural features of the myocardium and the implanted patch in the tissue-mimicking gel. For visualization of these features, PCI-CT offered a significantly higher performance than the dual absorption-phase and clinical magnetic resonance (3 T) imaging techniques. Furthermore, by reducing the total CT-scan time and ROI, PCI-CT was examined for lowering the effective dose, meanwhile without much loss of imaging quality. In effect, the higher soft tissue contrast and low-dose potential of PCI-CT has been used along with an acceptable overall animal dose to achieve the high spatial resolution needed for cardiac implant visualization. As a result, PCI-CT at the identified imaging parameters offers great potential for 3D assessment of microstructural features of hydrogel cardiac patches.

1. Introduction

Cardiac tissue engineering aims to develop implantable engineered constructs for myocardial infarction repair. Hydrogels have been extensively used in the development of functional cardiac constructs because of their ability to support cell growth (Izadifar *et al.*, 2014*a*,*b*) and stimulate vascularization, extracellular matrix secretion and cell alignment through hydrogel three-dimensional (3D) bioprinting (Izadifar *et al.*, 2014*a*, 2017).

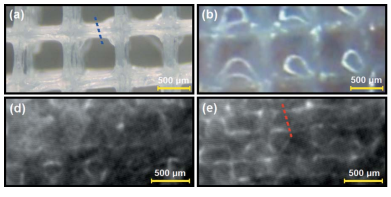

The visualization of hydrogel-based cardiac constructs is essential for longitudinal studies of cardiac tissue regeneration. However, examination using conventional histological and imaging methods is destructive, for which the animal must be euthanized. The development of non-invasive, quantitative and longitudinal imaging methods for assessment of 3D microstructures of the implanted cardiac constructs is a strategic priority in cardiac tissue engineering. Magnetic resonance imaging is limited by poor spatial resolution. Ultrasound is limited by penetration depth especially if a high spatial resolution is required. Microcomputed tomography (μCT) possesses high spatial resolution with deep tissue penetration but it only relies on X-ray absorption contrast. Since hydrogels are low-density biomaterials with weak X-ray linear attenuation coefficients, conventional μCT provides little or no information on the construct microstructural properties.

Unlike X-ray absorption-based imaging methods, phase-contrast imaging (PCI) techniques have shown promise for soft-tissue imaging. Propagation-based PCI, also known as in-line PCI, is an X-ray phase-sensitive imaging technique based on X-ray refraction rather than the X-ray linear attenuation coefficient of soft tissues. The advantage of X-ray PCI over absorption-based imaging stems from the fact that soft-tissue refractive index variations are typically greater than the X-ray absorption coefficient variations by orders of magnitude (Lewis, 2004). With ever-improving high-resolution X-ray detectors, highly brilliant and coherent synchrotron X-ray PCI offers great promise for visualization and non-invasive assessment of soft tissues that possess very similar X-ray absorption coefficients.

Several groups have applied X-ray in-line PCI for visualization of tissue-engineered constructs such as polyethylene glycol in water (Brey *et al.*, 2010), poly(glycolic acid)-polyethylene glycol *in vitro* (Albertini *et al.*, 2009), poly(α-hydroxy-ester) in water (Appel *et al.*, 2012), poly(L-lactide) and chitosan scaffold in air and water (Zhu *et al.*, 2011) and polycaprolactone-alginate *in vitro* (Olubamiji *et al.*, 2016). Although the potential of PCI for visualization of soft tissue has shown promise by these previous studies, little has been published for hydrogel-based cardiac tissue engineering. In addition, most of the studies have investigated planar PCI, for which the imaging performance dramatically declines with increasing thickness and complexity of the sample. Combined with computed tomography (CT), PCI-CT may overcome the limitations for visualization of microstructural features of implanted hydrogel-based cardiac constructs. However, compared with planar PCI, PCI-CT requires a much longer time for capturing serial planar X-ray images from which the 3D reconstruction is done, which increases the delivered dose and time. Therefore, the PCI-CT imaging parameters need to be adjusted and optimized to provide high-quality images at low absorbed dose, thus allowing for potential application of this imaging technique towards live animal imaging. To our best knowledge, there is no prior report on low-dose propagation-based PCI-CT for visualization of implanted soft cardiac constructs. As envisioned, this study aimed to develop a low-dose 3D in-line synchrotron-based PCI-CT to visualize a dual-component fibrin–alginate cardiac patch implanted in a rat model through an *ex vivo* study.

2. Materials and methods

2.1. 3D-plotting of cardiac patch

Using a 3D-bioplotter fabrication system (Envisiontec GmbH, Gladbeck, Germany) (Fig. 1*a*), sodium alginate (Sigma-Aldrich Co., Saint Louis, MO, USA) [2.5% weight per

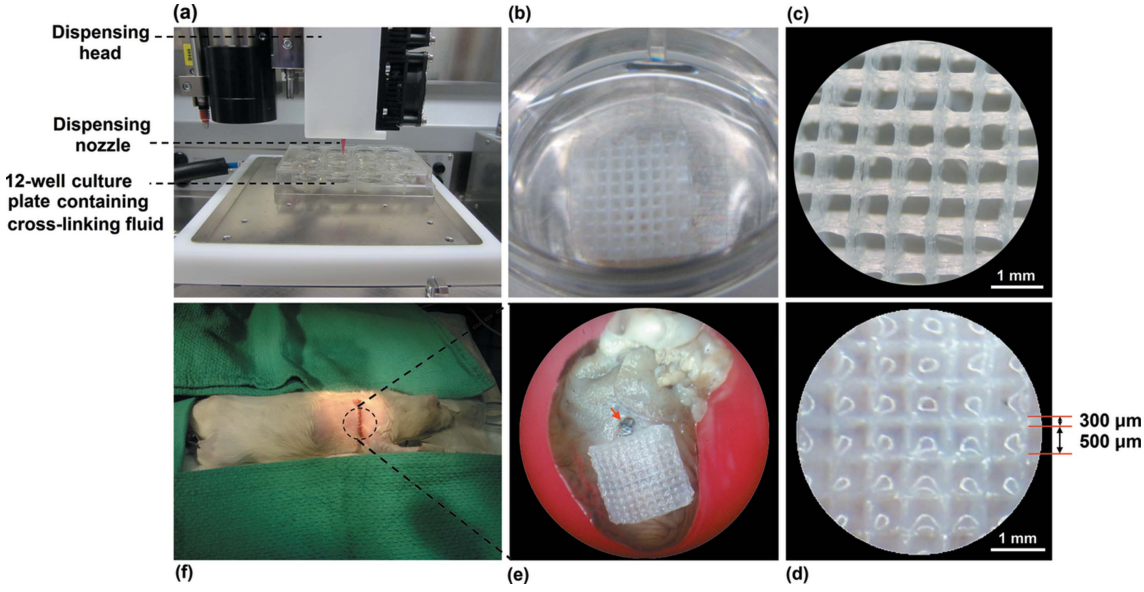

Figure 1
Fabrication of an implantable dual-material cardiac patch composed of a 3D-printed porous alginate filled with fibrin. Using a 3D-bioplotter (*a*) alginate (2.5%) strands are plotted layer by layer into the calcium chloride (*b*) in order to obtain a porous 3D structure with 0/90° printing pattern (*c*) with a strand size of ∼300 μm and strand clearance of ∼500 μm filled with fibrin infusion (*d*) before implanting the patch proximal to the LAD ligature on the rat heart (*e*, *f*).

volume (*w*/*v*)] in sterile de-ionized water was printed into polyethyleneimine (PEI)-coated culture plate wells (Figs. 1*a*,1*b*) filled with cross-linking calcium chloride solution and 0.1% *w*/*v* PEI (Sigma-Aldrich Co., Saint Louis, MO, USA). The 3D constructs were fabricated with an overall size of 8 mm × 8 mm × 2.5 mm (W × L × H) with 0/90° perpendicular pattern of strands (Fig. 1c). The 3D plotting was performed at a dispensing head speed of 8 mm s^{-1} under a pneumatic pressure of 0.1 bar through a plastic cone tip dispensing needle (Fig. 1*a*) of 250 µm (EFD Nordson Corp., Westlake, OH, USA) at strand spacing (center to center) of 700 µm. Sterile fibrinogen (8 mg ml^{-1}) and thrombin (2 U ml^{-1}) (Baxter Healthcare Co., Westlake Village, CA, USA) were mixed by pipetting in a vial and quickly infused into the pores of the 3D construct before the fibrin gel set (Fig. 1*d*), forming the so-called 'dual-component' patches for the subsequent studies.

2.2. Surgical procedure and implantation of cardiac patch

Male Lewis rats (~200 g) were anesthetized with a mixture of oxygen and isoflurane (2.5%), intubated and mechanically ventilated at 70 breaths per minute and 2 ml tidal volume. Following an anterior thoracotomy through the fourth intercostal space, the heart was exposed, the pericardium removed and the proximal left anterior descending (LAD) coronary artery ligated with a 7–0 silk suture (red arrow in Fig. 1*e*) under a surgical microscope. The alginate–fibrin patch was then implanted on the myocardium proximally below the LAD ligature using surgical fibrin glue (Fig. 1*e*). The intercostal space and skin were closed using prolene sutures (Fig. 1*f*). The rat was housed under standard conditions for seven days before being euthanatized prior to synchrotron PCI-CT imaging. The experiments were conducted in compliance with the guidelines and ethics set by Canadian Council on Animal Care and the animal use protocol (ethical permission number 20140094) approved by the Animal Research Ethics board of the University of Saskatchewan.

2.3. Synchrotron X-ray PCI-CT of the implanted cardiac patch

2.3.1. Sample preparation for imaging. The thoracic cavity was exposed, followed by clipping of the vena cava, pulmonary vein and artery and aorta in order to avoid trapping air bubbles in the heart chambers during the heart excision. Agar gel that exhibits absorption and scattering characteristics similar to soft tissues was used as the soft-tissue-mimicking medium (Liliana *et al.*, 2014) fully embedding the heart in a plastic sample holder tube. The heart was carefully excised and immediately laid on the surface of the agar gel inside the sample holder. Clips were removed and the tube was carefully filled with low-melting-point agar (Sigma-Aldrich Co., St Louis, MO, USA) solution (1% *w*/*v*) at 39–40°C, ensuring there were no trapped bubbles around the patch and the surrounding tissue. The agar was allowed to set for 15 min on ice prior to positioning the tube on the CT imaging stage for PCI-CT imaging.

2.3.2. Propagation-based PCI-CT set-up and parameters. The PCI-CT was performed at the Biomedical Imaging and Therapy bending-magnet (BMIT-BM) beamline, Canadian Light Source (CLS), Saskatoon, Saskatchewan, Canada. Fig. 2 shows a schematic diagram of the PCI-CT set-up at BMIT-BM. Upstream of the imaging stage, the white beam was shaped using slits to provide sufficient horizontal beam width, and then attenuated through an aluminium filter to reduce the power loading and thermal drift of the monochromator. A highly collimated monochromatic X-ray beam at 25 keV was chosen using a Si (2, 2, 0) double-crystal monochromator. Passing through the ion chamber, the X-ray beam illuminates

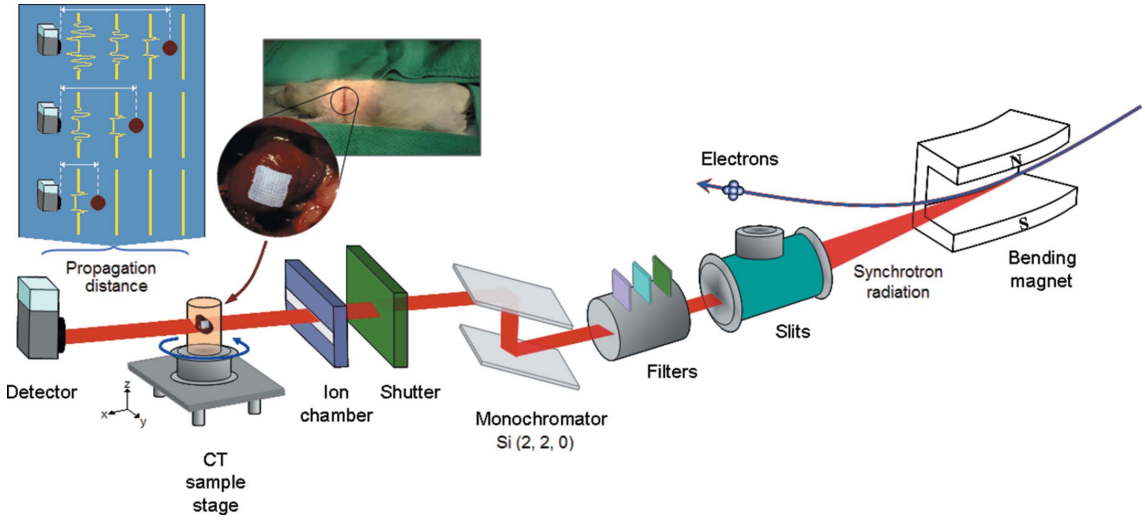

Figure 2
Schematic diagram of the synchrotron PCI-CT imaging set-up with adjusted phase propagation distance at the BMIT bending-magnet beamline. The deflection of the electron trajectory at the bending magnet provides synchrotron light, so-called 'white beam', that is shaped by slits and filtered. The double-crystal monochromator provides a monochromatic X-ray beam (25 keV) that passes through the shutter and the ion chamber to be used for imaging. The collimated monochromatic X-ray beam travels through the heart and implanted patch embedded in the tissue-mimicking gel. The small phase shifts attributed to the structural features are developed in free propagation distance after the sample and the accentuated phase contrast is recorded by the detector at three sample-to-detector distances. PCI-CT tomography projections are collected by rotating the sample in the beam.

the sample at a beam width and height of 25.6 mm and 4.0 mm, respectively. The X-ray images were collected using a Hamamatsu ORCA detector (Hamamatsu Photonics KK, Hamamatsu, Japan) with an effective pixel size of 12.5 µm, after travelling over a propagation distance, which was optimized by displacing the sample towards or away from the detector. For examining the effect of the propagation distance on the imaging quality, in this study PCI-CT was performed at three distinct phase propagation distances of 22 cm, 76 cm and 147 cm.

Unlike conventional CT in a clinic, where the patient is stationary and the X-ray source and detectors are rotated, for synchrotron X-ray in-line PCI-CT the source of the X-ray beam remains stationary while the sample stage is rotated. The rotational increments of the sample stage were set as 0.06, 0.12, 0.18 and 0.24°, which resulted in four levels of CT-acquisition time per slice of the sample over 180° in a step-shoot fashion. The area of the region of interest (ROI) was adjusted using slits. The collected planar X-ray projections at different distances of phase propagation, CT-acquisition times and the area of the ROI were normalized with flat and dark images. The background-corrected images were then used for phase-retrieval and CT image reconstruction.

2.4. Retrieving phase information of PCI-CT images

Phase-retrieval was performed to extract phase information allowing for edge-enhanced visualization of the boundaries of the object features. In this study, the phase-attenuation duality Bronnikov algorithm (PAD-BA) that utilizes a single propagation distance for objects with weak X-ray absorption and phase-attenuation duality was used for phase retrieval (Liliana *et al.*, 2014). PAD-BA was implemented by using phase-sensitive X-ray image processing and tomography reconstruction (PITRE) software to retrieve phase information as reported by Chen *et al.* (2012),

$$\varphi_\theta(x,y) = F^{-1}\left(\frac{F\left(I_{z,\theta}-1\right)/2}{\left\{\cos[\pi\lambda Z(\xi^2+\eta^2)]+\sin[\pi\lambda Z(\xi^2+\eta^2)]\right\}/(\alpha/\beta)}\right), \quad (1)$$

where F denotes the Fourier transform, λ is the wavelength, Z is the sample-to-detector propagation distance, ξ and η are the spatial frequencies in Fourier space corresponding to the coordinates of x and y in real space, α and β are the X-ray refractive and absorption indices, θ is the tomography rotation angle, I is the photon intensity and $\varphi_\theta(x,y)$ is the phase corresponding to the image coordinates of x and y at the tomography angle of θ.

A sensitivity analysis was performed to approximate α/β of the sample. Considering that myocardium is a soft tissue and the implanted cardiac patch is largely composed of water, an initial α/β value of 2180 corresponding to the absorption and refractive indices of water ($\alpha = 0.14\times10^{-6}$, $\beta = 0.0658\times10^{-9}$) was used for assessing the width of the fringes at the boundaries with respect to α/β ranging from 1500 to 4000. The best α/β value was determined based on the variation of fringe size with α/β value at the myocardium and patch boundaries. Applying the filtered back-projection algorithm, the dual phase-absorption images (phase-nonretrieved images) and phase-retrieved images were reconstructed. The signal intensities of the phase-retrieved and dual phase-absorption (phase-nonretrieved) CT reconstructed images were corresponding to apparent refractive index ($\bar{\alpha}$) and apparent attenuation coefficient ($\bar{\mu}$), respectively. The PAD modified Bronnikov algorithm (PAD-MBA) was also applied for phase retrieval of single planar PCI of the myocardium and the implanted patch compared with PAD-BA.

2.5. Magnetic resonance imaging (MRI) of the heart and cardiac patch

Following synchrotron PCI-CT experiments, the sample of heart with cardiac patch embedded in agar was imaged by a clinical MRI unit at the Royal University Hospital, Saskatoon, Canada. MRI was performed on a 3 T Siemens MAGNETOM Skyra scanner (Siemens Healthcare GmbH, Erlangen, Germany) equipped with a gradient system capable of 45 mT m^{-1} maximum strength. The heart sample-containing tube was stabilized in a MRI-compatible wrist holder for planar scanning along the patch longitudinal axis. T2 measurements were performed at 25°C with a T1-weighted susceptibility-weighted imaging (SWI) sequence (TE1 = 7.01 ms, TE2 = 20 ms) at a repetition time (TR) of 28 ms, number of echo images of 2, field of view (FOV) of 50 mm × 50 mm, slice thickness of 0.4 mm, and resolution of 128 µm × 128 µm × 44 µm. Relaxation data were analyzed using the VE11A software (Siemens AG, Erlangen, Germany).

2.6. X-ray radiation dose assessment and low-dose PCI-CT

The synchrotron radiation dose rate in air is typically measured using a calibrated ion chamber at BMIT-BM (Canadian Light Source, 2015). To determine the dose rate variations over the CT scan during which the storage ring current changes, a multiple regression equation that relates dose rate to the storage ring current (150–250 mA) and photon energy (20–35 keV) was developed,

$$\vartheta^\bullet = 198.103 - 10.87E + 0.163\Theta + 0.13E^2, \quad (2)$$

where E is the X-ray energy (keV), Θ is the storage ring current (mA) and $\vartheta^\bullet$ is the dose rate in air (mGy s^{-1}). For an X-ray energy of 25 keV at which the dose rate only depends on the storage ring current, equation (2) results in a mean prediction error of 4% and coefficient of determination of 0.995, where the variation of dose rate with time during PCI-CT scan can be described as

$$\frac{\partial\vartheta^\bullet}{\partial t} = \frac{\partial\vartheta^\bullet}{\partial\Theta}\frac{\partial\Theta}{\partial t}. \quad (3)$$

Evaluating equation (3) based on the first derivative of equation (2) and recorded data of the storage ring current during the PCI-CT scan, and taking the integral of (3) results in

$$\vartheta^\bullet = \vartheta_0^\bullet - 0.5008\tau, \quad (4)$$

where $\vartheta_0^{\bullet}$ is the initial value of the dose rate in air corresponding to the ring current at the beginning of the PCI-CT scan, and τ is the total exposure time defined by

$$\tau = (\tau_c + \tau_r) N, \tag{5}$$

where τ_c is the time for signal capturing by the detector per projection, τ_r is the time for the angular rotation step, and N is the total number of tomography projections. The total X-ray absorbed dose of the PCI-CT was evaluated as

$$D = N (\tau_c + \tau_r) \vartheta^{\bullet}, \tag{6}$$

where D is the total absorbed dose in air at the entrance surface (mGy). To provide clinically interpretable evaluation of the radiation dose, the absorbed dose was weighted with respect to radiobiological risks of the exposed tissue to estimate the effective dose equivalent in Sievert (Sv) as

$$Sv = D\, W_r\, W_t, \tag{7}$$

where W_r and W_t are the radiation weighting factor, that is equal to 1 for X-ray photons, and the tissue radiosensitivity weighting factor, respectively. A cardiac tissue radiosensitivity weighting factor of 0.12 (SCENIHR, 2012) was used for estimation of the effective dose.

At the dose rate assigned by the chosen X-ray energy (25 keV) and the storage ring current, the total delivered dose was investigated at three levels of the area of the ROI (~100, 6, 3 mm^2) and four levels of CT-scan time corresponding to tomography projections of 3000, 1500, 1000 and 750. The beam dimensions, which can be adjusted using fully X-ray absorbing slits, were adjusted to provide a reduced ROI. The combination of decreased CT-scan time and reduced ROI was analysed with the associated image quality criteria to identify optimum imaging parameters for an effective low-dose PCI-CT.

2.7. Qualitative and quantitative criteria for assessing image quality

The following image quality criteria were used: image correlation coefficient (r), peak of signal-to-noise ratio (PSNR), contrast-to-noise ratio (CNR) and structural similarity (SSIM) index, to compare CT images of the heart and implanted patch associated with different levels of delivered dose. The image quality criteria per unit delivered dose per pixel were defined as

$$\overline{\mathrm{SSIM}} = \frac{(P_{xy})^2 (2\mu_{\mathrm{ROI}}\mu_b + C_1)(2\sigma_{\mathrm{ROIb}} + C_2)}{S_{\mathrm{ROI}}(\mu_b^2 + \mu_{\mathrm{ROI}}^2 + C_1)(\sigma_b^2 + \sigma_{\mathrm{ROI}}^2 + C_2) D}, \tag{8}$$

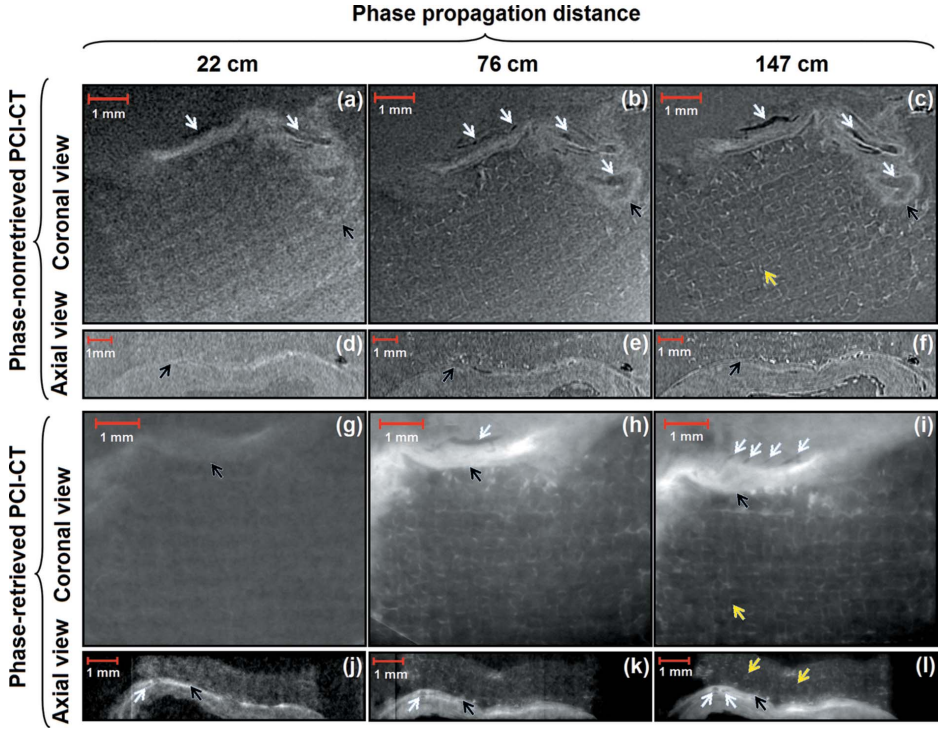

Figure 3
Phase-nonretrieved and phase-retrieved PCI-CT images of coronal (*a–c*, *g–i*) and axial (*d–f*, *j–l*) slices of the cardiac patch implanted on the rat myocardium at three phase propagation distances of 22 cm, 75 cm and 147 cm.

$$\overline{\mathrm{CNR}} = \frac{(P_{xy})^2 \sigma_{\mathrm{ROI}}}{S_{\mathrm{ROI}} \sigma_b D}, \tag{9}$$

where $\overline{\mathrm{SSIM}}$ and $\overline{\mathrm{CNR}}$ are the normalized SSIM index and CNR per unit absorbed dose per image pixel, S_{ROI} is the area of the ROI, D is the total absorbed dose in air at the entrance surface, μ_{ROI} and μ_b are the mean intensity of image signals of the ROI and background, respectively, σ_{ROI} and σ_b are intensity standard deviations of the image signals of the object ROI and background with equal surface area, respectively, σ_{ROIb} is the inner product of the standard deviations, C_1 and C_2 are stability constants, and P_{xy} is the pixel size (mm). The apparent refractive index profiles across the ROI of the implanted cardiac patch were used to identify the boundaries between fibrin-filled pores and alginate strands and quantitatively evaluate the features of the patch compared with the actual values measured from stereomicroscope images.

3. Results

3.1. Effect of the phase propagation distance of the PCI-CT

A sensitivity analysis of the phase retrieval revealed that the width of the phase contrast fringes at the boundaries between myocardium and implanted patch decreased as α/β was increased from 1500 to 3500. A further increase in α/β resulted in no significant improvement in the width of the fringes; thus, α/β of 3500 was applied to PAD-BA for the phase retrieval in the study. Fig. 3 depicts the axial and coronal slices associated with phase-attenuation duality (phase-nonretrieved) and

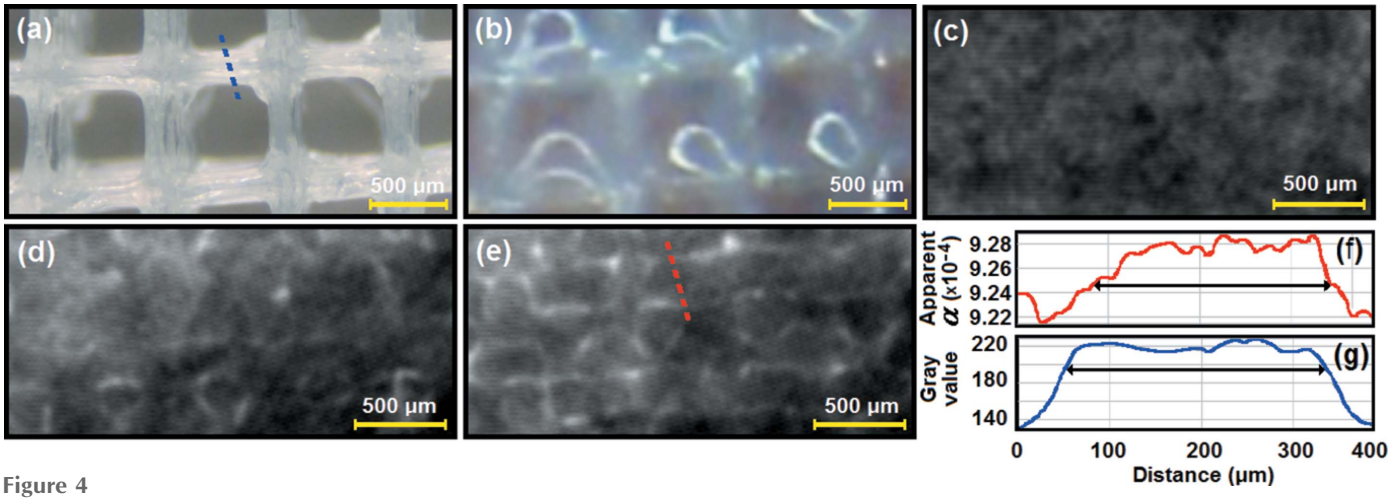

Figure 4
Comparison of structural similarity between stereomicroscope images of the 3D-printed alginate strands (*a*), dual component alginate–fibrin structure (*b*), and the coronal slice of the phase-retrieved images from PCI-CT at a phase propagation distances of 22 cm (*c*), 76 (cm) and 147 cm (*e*) at $\alpha/\beta = 3500$; a quantitative comparison of the alginate strand thickness (black arrows on the graphs) evaluated from the PCI-CT at a phase propagation distance of 147 cm (*f*) and the corresponding measured value from the stereomicroscope image (*g*).

phase-retrieved images of the implanted patch on the myocardium at three phase propagation distances. As the phase propagation distance increases from 22 cm to 147 cm, the edge illumination at the interface between the alginate strands and fibrin-filled spaces (yellow arrows) and between the patch and the myocardium (black arrows) significantly improves (Figs. 3*a*–3*c*, 3*g*–3*i*). At a distance of 147 cm, the phase-retrieved images clearly depict the structural and morphological information of the patch (Fig. 3*i*) including the vertically assembled alginate strands that demonstrate circular cross sections (yellow arrows) (Fig. 3*l*). Moreover, the microvessels (yellow arrows) can be clearly identified from the coronal views at a propagation distance of 147 cm (Figs. 3*c*,3*i*).

Figs. 4(*a*) and 4(*b*) depict the structural details of the 3D-printed alginate construct and the alginate–fibrin patch, respectively. As the propagation distance increases from 22 cm (Fig. 4*c*) to 76 cm (Fig. 4*d*) and 147 cm (Fig. 4*e*), the edge illumination improved so that the boundaries between alginate and fibrin can be clearly identified and the thickness of the strands can be characterized from the PCI-CT slice (Fig. 4*e*). Fig. 4(*f*) illustrates the apparent refractive index profile across the alginate strand (Fig. 4*e*), indicating a strand thickness of ~300 µm (Figs. 4*e*,4*f*) which is in agreement with the strand thickness evaluated from the intensity profile of the stereomicroscope image (Figs. 4*a*,4*g*). It is noted that there is an approximately 20% increase in the strand thickness (~300 µm) as compared with the internal diameter of the dispensing needle (250 µm) used for printing the strands of the cardiac patch, which is mainly due to the spreading or stretching of strands during their cross-linking process.

3.2. Planar PCI to assess the patch implantation

Fig. 5 shows the planar PCI (single projections) of sagittal and axial views of a ROI of the heart at the phase propagation distance of 147 cm. Figs. 5(*a*) and 5(*b*) depict the sagittal and axial phase-absorption duality planar images, respectively, where the myocardium (yellow arrows) and part of the aorta (blue arrows) boundaries can be identified. The edges of the left atrium appendage (green arrow) can be distinguished (Figs. 5*a*,5*b*); however, the profiles of the apparent attenuation coefficient across the region of the patch implantation show no significant contrast for locating the implanted patch (Figs. 5*g*,5*h*). In contrast, the phase-retrieved planar images from PAD-MBA (Figs. 5*c*,5*d*) and PAD-BA (Figs. 5*e*,5*f*) depict boundaries attributed to the edge enhancement of the myocardium (yellow arrows), patch (red arrows), appendage (green arrow) and aorta (blue arrow). The apparent refractive index profile (Fig. 5*i*) corresponding to the dashed line on the sagittal image (Fig. 5*c*) of the heart demonstrates a 'valley–hill' pattern which may represent the periodic alginate strands of the implant. The apparent refractive index profile (Fig. 5*j*) associated with the dashed line on the axial view (Fig. 5*d*) of the heart also indicates contrast attributed to the myocardium. Notably, PAD-BA results in better phase contrast of the implanted patch (Figs. 5*e*,5*k*) compared with PAD-MBA (Figs. 5*c*,5*i*), although both algorithms can retrieve phase contrast of the myocardium (yellow arrows) from the planar axial PCI (Figs. 5*c*–5*l*).

3.3. PCI-CT imaging performance compared with the clinical MRI

The MRI images provide no detailed information about the patch but only indicate the region of patch implantation (Figs. 6*a*,6*b*). The MRI horizontal long axis plane (Fig. 6*c*) is so poor that even chambers are unidentifiable. The magnetic resonance signal intensity profile across the patch suggests that MRI may only provide sufficient contrast for locating the implantation landmark but no details of the patch structure (Fig. 6*d*). The axial slice from phase-absorption duality PCI-CT of the patch clearly depicts the patch size and the strand nodes of the patch (Fig. 6*e*). The apparent attenuation coefficient profile across the patch and myocardium illustrates

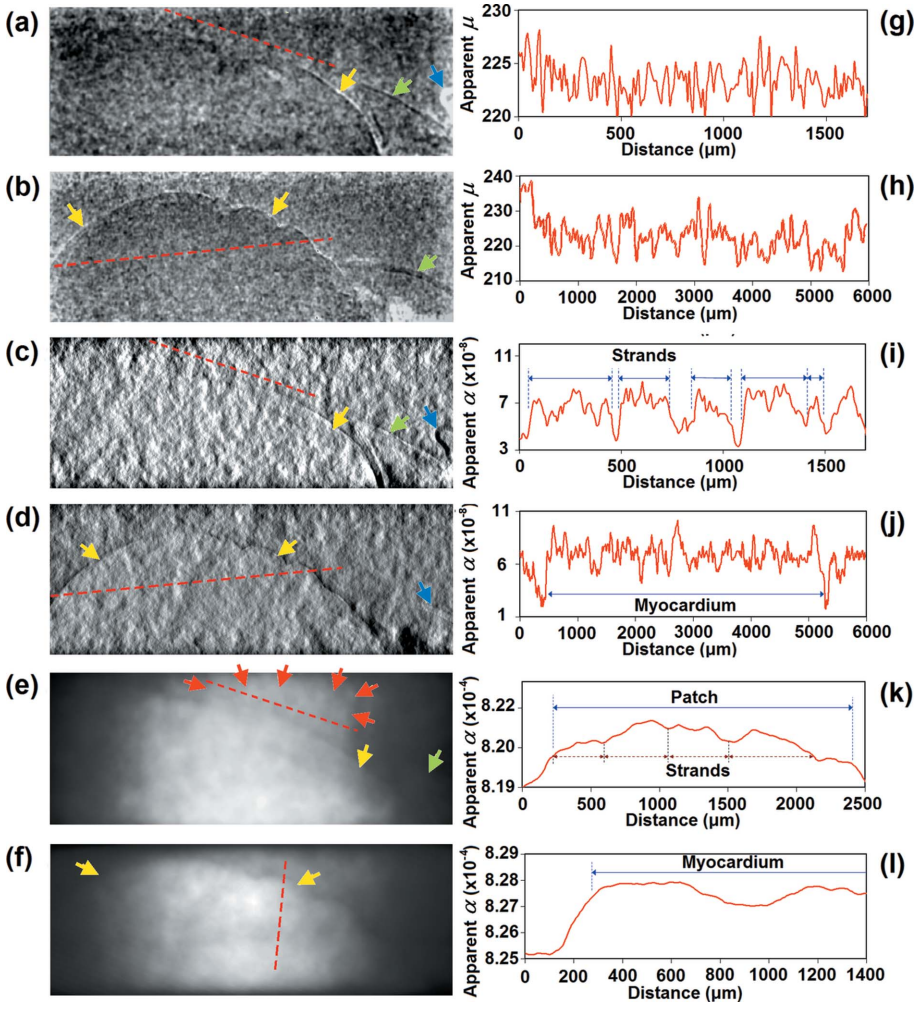

Figure 5
Single X-ray PCI projection (planar view) of sagittal (*a*,*c*,*e*) and axial (*b*,*d*,*f*) views associated with phase-nonretrieved (*a*,*b*) and phase-retrieved images from PAD-MBA (*c*,*d*) and PAD-BA (*e*,*f*) of the myocardium and the implanted patch, and the intensity profiles of the apparent attenuation coefficient (cm^{-1}) (*g*,*h*) and refractive index (*i*–*l*) corresponding to the dashed lines indicated on the images.

relatively sufficient contrast to identify alginate strands but hardly the exact boundary between the myocardium and the patch (Figs. 6*f*,6*h*). Also, the four-chamber long axial plane from phase-nonretrieved slices reveals some anatomical details that include left and right ventricles (red arrows), aorta (yellow arrow) and the right atrium (green arrow) (Fig. 6*g*). The axial slice of the phase-retrieved images not only provides the size, geometry and the strand nodes but clearly visualizes the thickness and orientation of the strands with quantifiable fibrin-filled pores (Fig. 6*i*). Unlike MRI and the phase-absorption duality PCI-CT, the phase retrieval significantly improves the contrast between myocardium and implanted patch, thus being able to assess the patch attachment to the myocardium post implantation (Fig. 6*j*). Notably, the apparent refractive index profile across the patch and myocardium clearly shows the contrast between the implanted patch and the native myocardium, as well as the information associated with the myocardium microvessel and patch strands (Fig. 6*l*). Furthermore, the axial plane reveals anatomical details of the interior heart such as atriums (green arrows), mitral valve (blue arrow), tendinous cords of the tricuspid valve (pink arrow), left and right ventricles (red arrows), aorta (yellow arrow) and the left atrium appendage (white arrow) (Fig. 6*k*).

It should be noted that for PCI there is a need for sufficiently small pixel size to capture the X-ray intensity variations arising from the X-ray refractive index (real part) variations within the patch. These variations redirect the X-ray light and create regions of X-ray intensity increase and decrease, accentuating microstructural features of the patch. The spatial extent of this X-ray light 'redirection' is quite small given the small variations of the refractive index within the patch. Typically, the X-ray refractive index deviation from 1 in soft tissues is of the order of 10^{-7} and thus refraction angles are also small and of the order of fractions of a microradian. Also, the X-ray source size needs to subtend a comparably small angle at the object and detector so that the intensity variations can be resolved. All of these conditions can be met with a synchrotron source where the combination of source size and distance from the source allow the resolution of the intensity variations.

The patch microstructure (Fig. 7*a*) and the associated periodic 'hill–valley' pattern of the apparent refractive index profile associated with the fibrin–alginate periodic structure (Fig. 7*b*) can be seen in the axial slice of the phase-retrieved PCI-CT image. The size of the fibrin-filled pores and alginate strands can be approximated from the apparent refractive index profile (Fig. 7*b*), with their values of ∼250 and 400 µm, respectively. Notably, these identified values are in agreement with those measured from stereomicroscope images, *i.e.* ∼300 and ∼500 µm. Compared with the phase-retrieved image, the axial plane (Fig. 7*c*) and the associated apparent absorption coefficient profile (Fig. 7*d*) from the phase-absorption duality PCI-CT suffers from insufficient contrast, making it very difficult to morphologically and quantitatively assess the patch microstructure.

3.4. Low-dose PCI-CT imaging

Figs. 8(*a*)–8(*d*) depict the volume rendered images utilizing 3000, 1500, 1000 and 750 tomography projections, respectively. The patch dimensions and the strand orientations, and some anatomical details such as the left atrium appendage (yellow

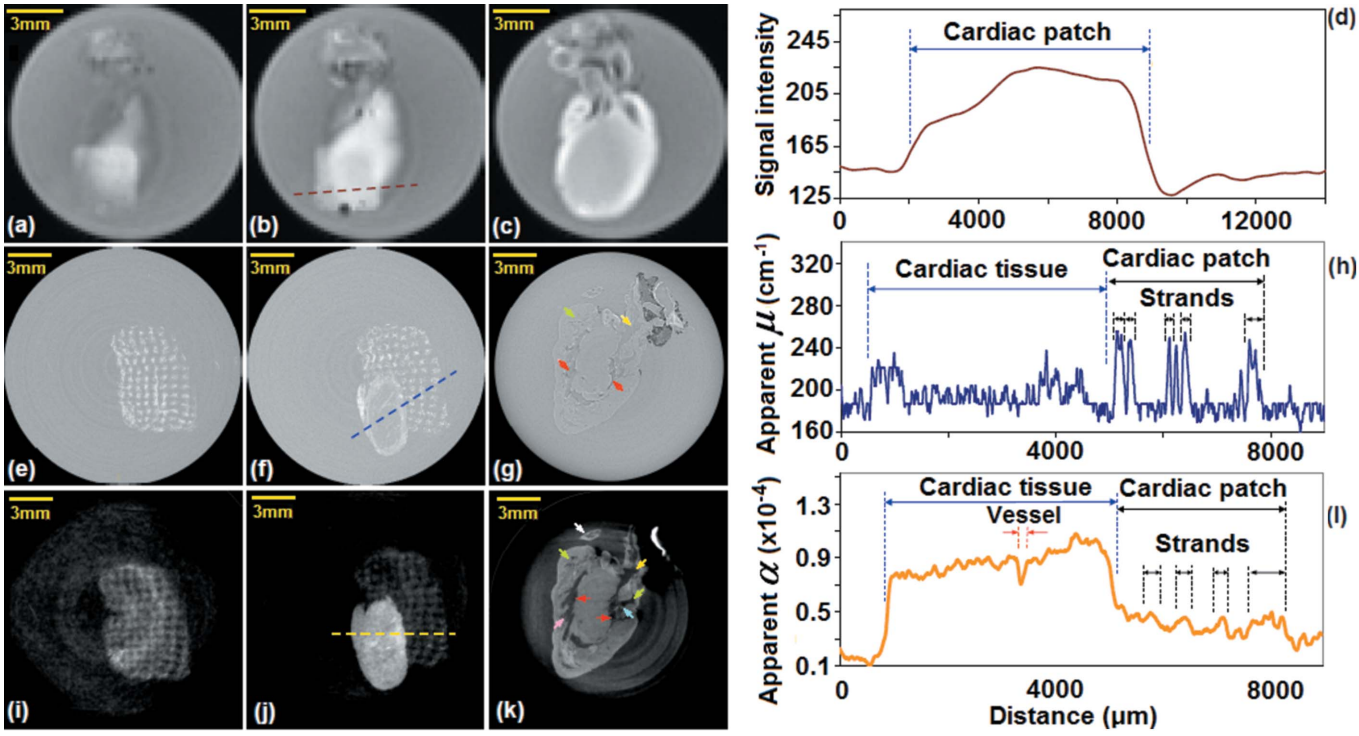

Figure 6
Coronal slices and signal intensity profile from MRI images (*a*–*d*) compared with the corresponding slices from phase-nonretrieved (*e*–*h*) and phase-retrieved PCI-CT images (*i*–*l*) of the heart and the implanted patch.

arrow), microvessels (red arrows) and the ligature (suture) (blue arrow) can be seen in the images using 3000 projections (Fig. 8*a*). The anatomical and structural features remain relatively distinguishable at reduced 1500 projections (Figs. 8*b*,8*f*). At 1000 tomography projections, it becomes difficult to identify the microvessels although the patch microstructure can be visualized (Figs. 8*c*,8*g*). Despite the poor resolution provided by 750 tomography projections, the suture (blue arrow), appendage (yellow arrow) and a few microvessels (red arrows) are identifiable (Fig. 8*h*) and the strand orientations of the patch and the area of the implantation can be approximated (Figs. 8*d*,8*h*).

A comparison between axial slices of the patch corresponding to the full dataset and the reduced tomography projections suggests that the key structural features of the patch remain identifiable with the reduced number of tomography projections despite the decreased spatial resolution (Figs. 8*e*–8*h*). Anatomical features such as the internal structure of the appendage (yellow arrow) and microvessels (red arrows) can also be distinguished from the surrounding tissue at the lower CT-scan times corresponding to the reduced number of tomography projections compared with the standard PCI-CT utilized 3000 projections (Figs. 8*i*–8*l*).

The apparent refractive index profiles corresponding to the blue line shown in Figs. 8(*i*)–8(*l*) indicate that the phase contrasts of the anatomical features are sufficient to distinguish myocardium and the patch at the reduced tomography projections (Figs. 8*m*–8*p*). Although two microvessels (red arrows in Fig. 8*p*) out of three can be located from the apparent refractive index profile associated with the image that utilized 750 tomography projections, 1500 and 1000 tomography projections

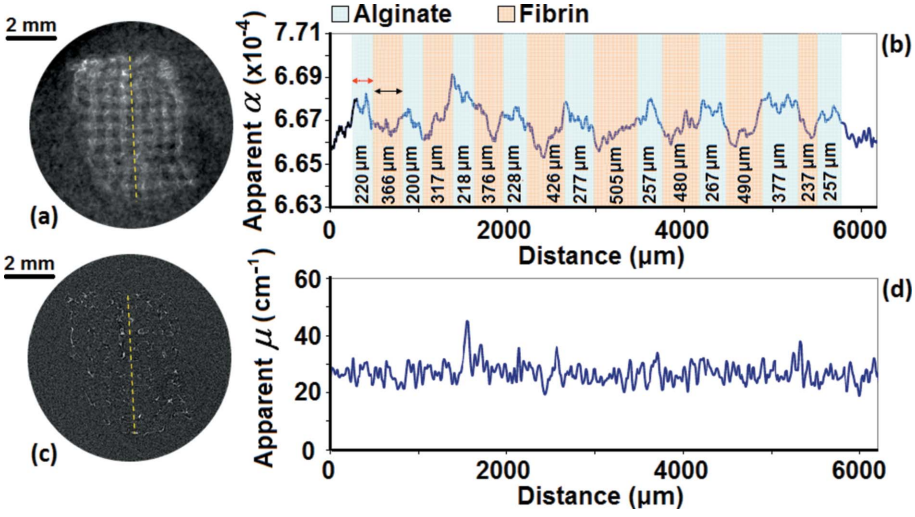

Figure 7
Quantitative assessment of the dual component implanted alginate–fibrin patch using a phase-retrieved (*a*,*b*) and phase-nonretrieved (*c*,*d*) horizontal long axis slice from the PCI-CT at a phase propagation distance of 147 cm and α/β of 3500.

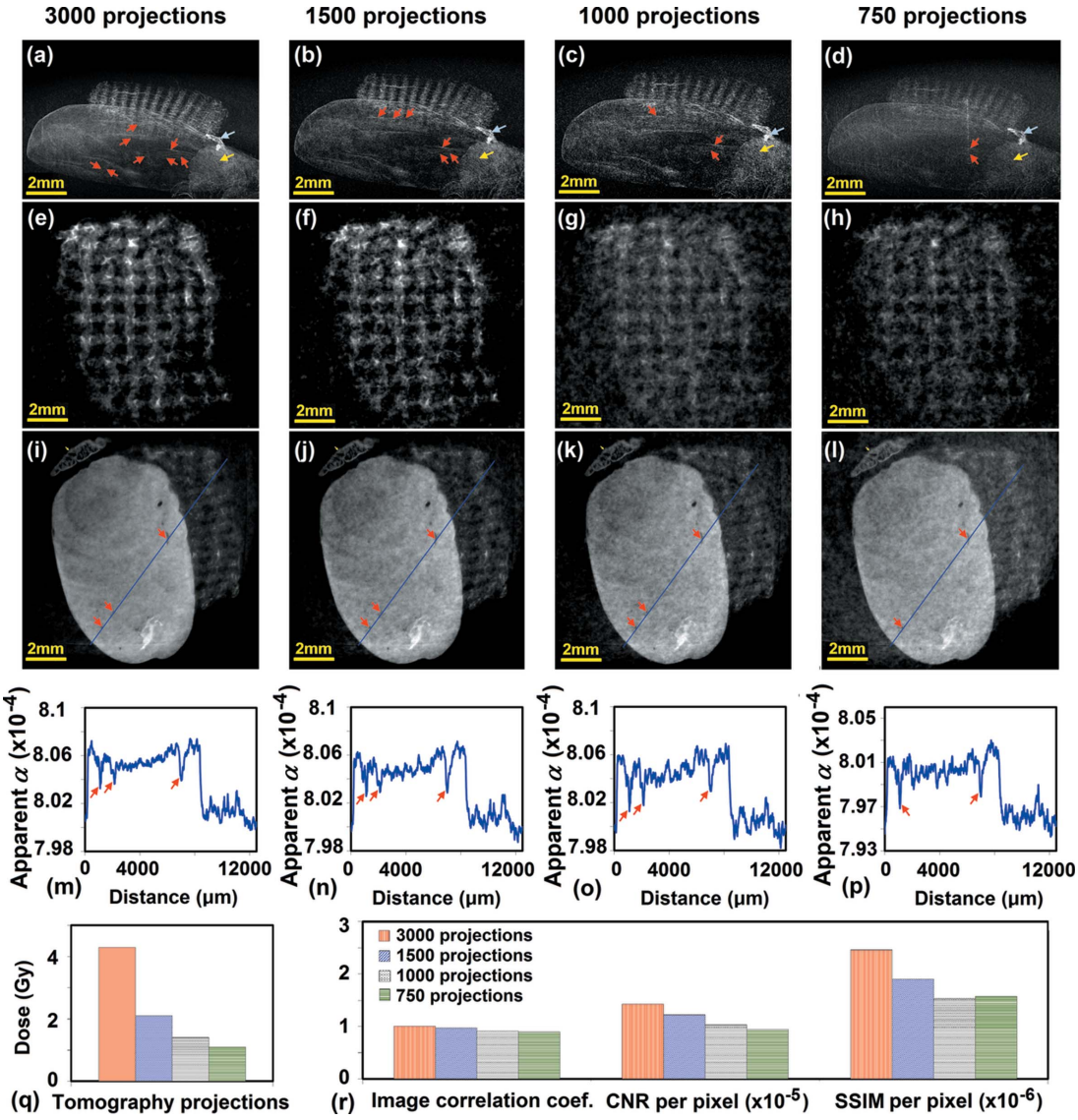

Figure 8
Sagittal views (*a*–*d*) of the volume rendered PCI-CT images of the heart and implanted cardiac patch, the horizontal long axial plane of the patch (*e*–*h*) attached to the myocardium (*i*–*l*), and the apparent refractive index profiles (*m*–*p*) corresponding to the blue lines indicated on the heart-patch PCI-CT images (*i*–*l*) that utilized tomography projections of 3000 (*a*,*e*,*i*,*m*), 1500 (*b*,*f*,*j*,*n*), 1000 (*c*,*g*,*k*,*o*) and 750 (*d*,*h*,*l*,*p*) to assess low-dose PCI-CT (*q*) and image quality criteria (*r*).

provide sufficient phase contrast to identify the three microvessels (red arrows) (Figs. 8*n*,8*o*).

Compared with the standard PCI-CT, the total delivered dose significantly declines when the tomography projections are decreased (Fig. 8*q*) but, notably, the image correlation coefficient and CNR per pixel are not significantly affected (Fig. 8*r*). Although the SSIM per image pixel is significantly decreased as a result of the reduced tomography projections, no significant difference in SSIM can be noted among the images associated with 1500, 1000 and 750 tomography projections (Fig. 8*r*).

Figs. 9(*a*)–9(*d*) depict the axial slices of the implanted patch for a ROI of 3 mm^2. Notably, the alginate strands of the patch remain identifiable and measurable from the images when the absorbed dose is reduced from 2 Gy (246 mSv) to 1 Gy (123 mSv), 0.6 Gy (82 mSv) and 0.5 Gy (62 mSv) corresponding to 3000, 1500, 1000 and 750 tomography projections, respectively (Figs. 9*a*–9*d*). The absorbed doses associated with 750–1500 tomography projections are within the range of the absorbed dose (0.5–1 Gy) of commercially available scanners operating in the 10–20 μm voxel range (Brouwers *et al.*, 2007; Pratt *et al.*, 2015). Coupled with the acceptable dose range, the refractive index profiles associated with the dashed line indicated on the images of patch strands (Figs. 9*a*–9*d*) reveals the periodic 'hill–valley' patterns attributed to the edge illumination of the alginate strands, which can be used for approximating the strand thickness (Figs. 9*e*–9*h*).

Table 1 presents the image quality criteria evaluated for different levels of PCI-CT doses. Obviously the image correlation coefficient decreases at the lower dose but the correlation coefficient generally remains above 0.8 with no significant change in PSNR except for the image at the ROI of

3 mm^2 and 750 tomography projections (Table 1). $\overline{\text{CNR}}$ and $\overline{\text{SSIM}}$ increase despite significant reductions in the absorbed dose, indicating that the image quality can be largely preserved at reduced doses (Table 1) which may be acceptable for *in vivo* cardiac CT scans of small animal models (Detombe *et al.*, 2013). The average strand thickness (d_s) and fibrin-filled pore size (d_f), which were evaluated from the phase-retrieved PCI-CT images, are generally consistent with measured values from stereomicroscope imaging (Figs. 4*a*,4*b*), suggesting that the PCI-CT may be implemented for quantitative assessment of the implanted cardiac patch.

Table 1
Quantitative criteria for image quality assessment and patch structural feature evaluation using PCI-CT at two levels of ROI and four levels of tomography projections.

S_{ROI} (mm^2)†	N	D (Gy)‡	r§	PSNR	$\overline{\text{CNR}}$ ($\times10^{-6}$)	$\overline{\text{SSIM}}$ ($\times10^{-6}$)	d_s (μm)¶	d (μm)††‡‡
1 × 6	3000	4.1	1	N/A‡‡	1.10	0.88	358	459
	1500	2.1	0.95	24.5	1.98	1.50	360	401
	1000	1.4	0.93	20.5	2.92	1.72	420	348
	750	1.0	0.83	20.7	3.71	2.37	442	332
1 × 3	3000	2.1	1	N/A††	12.51	1.18	319	433
	1500	1.0	0.89	23.0	21.63	2.37	351	436
	1000	0.6	0.80	20.4	30.84	3.55	413	358
	750	0.5	0.76	12.4	40.30	4.74	415	402

† Beam height × width. ‡ Total absorbed dose corresponding to S_{ROI} and N. § Image correlation coefficient between X-ray images and those acquired at 3000 tomography projections. ¶ Average alginate strand thickness of the implanted patch measured from the PCI-CT image. †† Average size of the fibrin filling spaces between alginate strands of the patch. ‡‡ The reference for evaluation of PSNR, r and SSIM.

4. Discussion

It has been shown that alginate offers a great cardiomyocyte encapsulation efficiency (Izadifar *et al.*, 2014*a*,*b*) and fibrin can significantly improve angiogenesis (Hadjipanayi *et al.*, 2015; Izadifar *et al.*, 2017). Inspired by these findings, it is rational to develop micro-patterned alginate–fibrin cardiac patches for cardiac tissue engineering. However, the ability to non-invasively and quantitatively visualize the alginate and fibrin is one of the key challenges. For this, PCI-CT has shown promise. The phase propagation distance has been shown to be critical and been optimized for achieving desirable phase contrast to depict microstructural features of the implanted cardiac patch, as illustrated in this study. It should be noted that both alginate and fibrin are made of more than 97% water, which provides very low density to the patch microstructure. As such, the patch microstructural features associated with the interface between the alginate strands and fibrin-filled pores produce very small phase shifts as the X-rays travel through the implanted patch, which is also true for the surrounding soft tissues such as microvessels. In synchrotron-based PCI-CT, the small phase shifts associated with microstructural features are magnified over the free propagation distance, producing sufficient phase contrast on the detector. Ideally, the phase propagation distance should allow the phase shift being developed to be as large as one pixel in size. If the phase distortion is smaller than the pixel size, phase shifts of multiple features are integrated within one pixel, making the projected boundaries fuzzy on the detector (Figs. 3*g*,4*c*). It should also be noted that the ability to visualize the fringes also depends on the X-ray source size. It is primarily the large distance between the X-ray source and the object/detector that allows

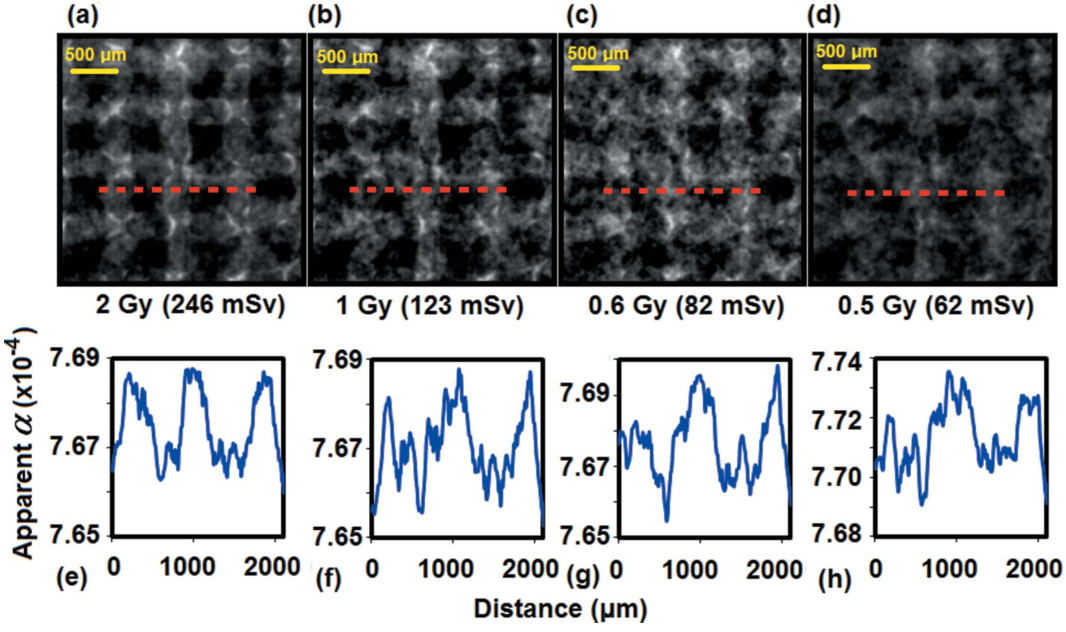

Figure 9
The patch structural feature assessment using PCI-CT imaging based on the combined effect of the reduced ROI (3 mm^2) at tomography projections of 3000 (*a*), 1500 (*b*), 1000 (*c*) and 750 (*d*) to quantitatively evaluate the size of strands and pores from the apparent refractive index profiles (*e*–*h*) associated with the dashed lines on the patch images.

these fringes to be seen. The phase effects described here also occur in any X-ray imaging system, but the effects are blurred by the short propagation distances (also known as 'unsharpness').

In this study, we illustrated that the best phase propagation distance for edge illumination of the alginate–fibrin interface of the patch was 147 cm among the three distances examined for an effective pixel size of 12.48 µm at BMIT-BM. Likewise, microvessel features illuminated at the phase propagation distance of 76 cm were measurable (∼25 µm) (Fig. 4*i*) at a sample-to-detector distance of 147 cm. Although a longer free propagation distance might improve the phase contrast of the microstructural features, projected boundaries may become blurry if the phase shift developments become larger than one pixel in size, which may occurr over a propagation distance longer than 147 cm.

At the optimum phase propagation distance, phase retrieval of the planar PCI provided sufficient contrast to identify the boundaries of the implanted patch distinguishable from the surrounding soft tissues (Figs. 5*h*,5*i*). This PCI capability, coupled with the extremely low delivered dose (∼1.5 mSv), offers a great potential for serial monitoring of the implanted patch; for example, to visualize degradation and to ensure that the patch is not detached or dislocated after surgery in a live animal study.

The phase-retrieved axial slice of the patch depicted no gap at the interface between the myocardium and the implanted patch, which is a non-invasive qualitative assessment of a successful implantation procedure. Furthermore, phase-retrieved PCI-CT slices enabled non-invasive quantitative assessment of the thickness of the alginate strands and the size of fibrin-filled pores which were consistent with the measured values from stereomicroscope imaging.

In addition to the qualitative and quantitative information of the patch, the phase-retrieved slices of the heart revealed descriptive anatomical features including the atrium appendage internal structure, mitral valve, tricuspid valve cords, aorta and myocardium microvessels. Notably, these microstructural and anatomical features of the patch and heart were achieved without the use of any contrast agent, suggesting that the PCI-CT is of great potential for non-invasive assessment of the patch structural changes, myocardium regeneration and vascularization in live animal studies for cardiac tissue engineering. It should be noted that for *in vivo* animal cardiac imaging the performance of the chest X-ray PCI can be affected by major variables such as scattering and photon starvation induced by the heart-surrounding lungs and ribs, respectively. In particular, lung alveoli are the major phase objects inducing significant X-ray phase shift due to the number of and refractive index shift between the tissue–air boundaries. The total amount of phase shift is the sum of phase shifts caused by all tissues including lungs, muscles, cardiac patch and the heart itself. Except for the ribs, all of these tissues contain low-Z elements so that the phase shift of each soft tissue is linearly related to its X-ray refractive index. The CT-scanning coupled with PCI that utilizes phase-retrieved tomography images from different angular projections enables mapping of the refractive indices of the tissues in the chest cavity (Masato *et al.*, 2012). We speculate that because the patch is implanted on the myocardium, rather than within the myocardium, the interface between the patch and the chest cavity may contribute to a phase contrast due to the significant variation of the refractive index between the patch and the cavity space. However, due to the air-filled alveoli that scatter X-rays, a significant contribution from this textured tissue will be expected for *in vivo* animal chest PCI-CT projections. The process of CT reconstruction resolves this issue. Unlike the aforementioned soft tissues surrounding the heart, ribs are the attenuating objects that are potential sources of photon starvation that can cause streaking artifacts in the reconstructed CT images. Based on the fact that the attenuation coefficient and penetration depth increases and decreases with photon energy, respectively, the use of higher X-ray energies will be applied to address the potential issue of photon starvation. In addition, the higher X-ray energy contributes to the absorbed dose reduction. This requires more work to assess in our future study.

Application of the PCI-CT technique to live animal studies relies not only on the image quality such as contrast and resolution but also on the total radiation dose. Since the absorbed dose is to an approximation inversely proportional to the fourth power of the pixel size (Ford *et al.*, 2003), for visualization of microstructural details of the cardiac hydrogel implants it is very difficult to reduce the dose without compromising the image quality. However, in this study, for a given storage ring current and a photon energy of 25 keV, the total CT-acquisition time and the area of the ROI were taken as the main factors to be optimized in order to reduce the absorbed dose without significant changes in the image quality criteria. The standard PCI-CT utilizing 3000 projections at a reduced ROI of 3 mm^2 delivered an absorbed dose of 2 Gy (256 mSv) which may be acceptable for *in vivo* imaging of small animal models. For mice models, the population-based lethal dose has been reported to range between 5 and 7.5 Gy (Clark & Badea, 2014). In terms of radiosensitivity, the thorax and abdomen are the most radiosensitive regions of an animal, with high radiation dose-induced pneumonitis as a lethal complication. Pneumonitis can arise in an animal when the thorax is exposed to over 1.9 Gy; however, studies have shown that rodents (*e.g.* mice) have survived X-ray exposures of about 3 Gy because of their ability to repair sub-lethal doses of radiation (Clark & Badea, 2014). Another study has concluded that an absorbed dose as high as 5 Gy during a longitudinal µCT study had no significant effects on the pulmonary and myocardial tissue of C57BL/6 mice (Detombe *et al.*, 2013). Results from these studies imply that the PCI-CT utilizing tomography projections of up to 3000 with a ROI area of 6 mm^2 may be acceptable for 3D visualization of cardiac hydrogel implants in rats (Table 1). In addition, for the PCI-CT utilizing tomography projections of 1500, 1000 and 750 at the ROI of 3 mm^2, the absorbed dose was reduced to a dose range between 0.5 and 1 Gy (Figs. 9*b*–9*d*). This range of µCT absorbed dose is similar to that of commercially available CT scanners (Pratt *et al.*, 2015) which are unable to visualize

structural details of soft hydrogel implants made of more than 97% water. The absorbed dose can be further reduced by use of higher X-ray energies and/or lower resolution imaging (*e.g.* 2×2 binning), which will be investigated in our future study.

5. Conclusion

In this study, a synchrotron propagation-based PCI-CT system has demonstrated promise for qualitative and quantitative assessments of implanted 3D-printed dual-component cardiac patches on a rat heart without use of a contrast agent. The 'low dose' potential of PCI coupled with an acceptable dose range for animal research allows sufficient resolution for monitoring the cardiac hydrogel implants. The microstructural features of fibrin and alginate were clearly visualized and quantitatively characterized from the phase-retrieved PCI-CT slices. The PCI-CT technique was also able to visualize some of the microvessels surrounding the implanted patch. Owing to the notable phase contrast at the optimized phase propagation distance, no contrast agent was needed for quantitative assessments of the patch and myocardium. By decreasing the area of the ROI and CT-scan time associated with reduced tomography projections, the absorbed dose was reduced without significant compromise to the imaging quality. In particular, the PCI-CT utilizing tomography projections of 750–1500 at a ROI of 3 mm^2 resulted in an absorbed dose ranging between 0.5 and 1 Gy acceptable for *in vivo* CT scanning in small animal models. Within this acceptable range of absorbed dose, the PCI-CT showed promise for quantitative visualization of strand thickness of the cardiac implant, which was consistent with actual strand measurements using stereomicroscope imaging.

In future experiments, the PCI-CT will be applied to the imaging of an implanted cardiac patch in a freshly euthanized rat allowing further refinement of the imaging parameters for the development of a robust gated PCI-CT for *in vivo* live animal studies.

Acknowledgements

The authors gratefully acknowledge Leona Boyer and Melanie Gibbons for assistance with anaesthesia and intubation during surgery, Mark Adam Webb and George Belev for assistance with preparation of the imaging stage at the CLS-BMIT, and Shawn J. Kisch for assistance with MRI at the Royal University Hospital. We also acknowledge that images presented in this paper were captured at the Canadian Light Source (CLS), which was supported by the Canadian Foundation for Innovation (CFI), Natural Sciences and Engineering Council of Canada (NSERC), the University of Saskatchewan, the Government of Saskatchewan, Western Economic Diversification (WED) Canada and Canadian Institutes of Health Research (CIHR).

Funding information

Funding for this research was provided by: Canadian Institutes of Health Research.

References

Albertini, G., Giuliani, A., Komlev, V., Moroncini, F., Pugnaloni, A., Pennesi, G., Belicchi, M., Rubini, C., Rustichelli, F., Tasso, R. & Torrente, Y. (2009). *Tissue Eng. C*, **15**, 403–411.

Appel, A. A., Larson, J. C., Somo, S., Zhong, Z., Spicer, P. P., Kasper, F. K., Garson, A. B., Zysk, A. M., Mikos, A. G., Anastasio, M. A. & Brey, E. M. (2012). *Tissue Eng. C*, **18**, 859–865.

Brey, E. M., Appel, A., Chiu, Y. C., Zhong, Z., Cheng, M. H., Engel, H. & Anastasio, M. A. (2010). *Tissue Eng. C*, **16**, 1597–1600.

Brouwers, J. E., van Rietbergen, B. & Huiskes, R. (2007). *J. Orthop. Res.* **25**, 1325–1332.

Canadian Light Source (2015). *BMIT-BM quality assurance for cycle 21*. Rev. A 26.5.1.5, 6. Canadian Light Source, Saskatoon, SK, Canada.

Chen, R.-C., Dreossi, D., Mancini, L., Menk, R., Rigon, L., Xiao, T.-Q. & Longo, R. (2012). *J. Synchrotron Rad.* **19**, 836–845.

Clark, D. P. & Badea, C. T. (2014). *Phys. Med.* **30**, 619–634.

Detombe, S. A., Dunmore-Buyze, J., Petrov, I. E. & Drangova, M. (2013). *Acta Radiol.* **54**, 435–441.

Ford, N. L., Thornton, M. M. & Holdsworth, D. W. (2003). *Med. Phys.* **30**, 2869–2877.

Hadjipanayi, E., Kuhn, P. H., Moog, P., Bauer, A. T., Kuekrek, H., Mirzoyan, L., Hummel, A., Kirchhoff, K., Salgin, B., Isenburg, S., Dornseifer, U., Ninkovic, M., Machens, H. G. & Schilling, A. F. (2015). *PLoS One*, **10**, e0135618.

Izadifar, M., Haddadi, A., Chen, X. B. & Kelly, M. (2014*b*). *Nanotechnology*, **26**, 012001.

Izadifar, M., Kelly, M. E. & Chen, X. B. (2014*a*). *Cardiovasc. Eng. Tech.* **5**, 281–307.

Izadifar, M., Kelly, M. E. & Chen, X. B. (2017). *Nanomedicine*, **11**, 3237–3259.

Lewis, R. A. (2004). *Phys. Med. Biol.* **49**, 3573–3583.

Liliana, A. L., Eugenio, T. G. & Rigoberto, O. P. (2014). *Open J. Radiol.* **4**, 44–52.

Masato, H., Kentaro, U. & Naoto, Y. (2012). *Biol. Open*, **1**, 269–274.

Olubamiji, A. D., Izadifar, Z., Zhu, N., Chang, T., Chen, X. & Eames, B. F. (2016). *J. Synchrotron Rad.* **23**, 802–812.

Pratt, I. V., Belev, G., Zhu, N., Chapman, L. D. & Cooper, D. M. (2015). *Phys. Med. Biol.* **60**, 211–232.

SCENIHR (2012). *Health effects of security scanners for passenger screening (based on X-ray technology)*, 26 April 2012, pp. 22–27. Scientific Committee on Emerging and Newly Identified Health Risks, European Union.

Zhu, N., Chapman, D., Cooper, D., Schreyer, D. J. & Chen, X. B. (2011). *Tissue Eng. C*, **17**, 1071–1080.